Surfaces and Interfaces 28 (2022) 101595

Contents lists available at ScienceDirect

Surfaces and Interfaces

journal homepage: www.sciencedirect.com/journal/surfaces-and-interfaces

Three-zone model for Ti, Al co-doped ZnO films deposited by magnetron sputtering

Florian Bocchese [a], David Cornil [b], Emile Haye [a], Jérôme Cornil [b], Stéphane Lucas [a,*]

[a] Laboratoire d'Analyse par Réactions Nucléaires (LARN), Namur Institute of Structured Matter (NISM), University of Namur (UNamur), 6 rue de Bruxelles, Namur B-5000, Belgium

[b] Laboratory for Chemistry of Novel Materials, Université de Mons (UMons), 20 Place du Parc, Mons B-7000, Belgium

ARTICLE INFO

Keywords:
Doped ZnO
Thin films
Magnetron sputtering
Optical properties
Structural properties
Morphological properties
Density functional theory

ABSTRACT

Al-doped ZnO is well known as an alternative Transparent Conductive Oxide (TCO) to Indium Tin Oxide (ITO). Recently, co-doped ZnO with Ti and Al (TAZO) have been explored to improve the conductivity while maintaining moisture durability and opto-electronic properties. In this context, the structural, morphological, and optical properties of TAZO films deposited by reactive magnetron are investigated by experiments and Density Functional Theory (DFT) simulations. The results show that TiO_2 units substitute Zn atoms in the ZnO wurtzite structure and, whatever the concentration of Ti, the formation of Al_2O_3 is taking place. In addition, a three-regime model as a function of Ti content is proposed to explain the evolution of the properties. First, for Ti content $\langle$ 2.2 at%, TiO_2 is incorporated by substitution of Zn by TiO_2 units in the ZnO network leading to a more oxidized Zn state and a hybridization between Zn_{4s} and Ti_{3d} orbitals. This opens the bandgap and increases the compressive stress of TAZO films. Between 2.2 at% and 7.0 at% of Ti content, cauliflower shape grains appear due to the compressive stress induced by small clusters of TiO_2. For Ti content $\rangle$ 7.0 at%, amorphous TAZO films are observed and are composed of TiO_2, Al_2O_3 and ZnO.

1. Introduction

Nowadays, most of the new technologies such as transparent transistors or solar control devices are typically exploiting transparent conductive oxides (TCO) deposited by magnetron sputtering [1–7]. Among the available TCOs, the one presenting the lower resistivity is Indium Tin Oxide (ITO) [8], but due to the high cost and limited availability of indium, alternative materials are necessary. For some potential applications, ZnO is a good alternative due to its non-toxicity, low-cost, abundancy and large bandgap (~3.27 eV). It is often doped with small active dopants such as Al to increase the charge carrier concentration. When synthetized by RF magnetron sputtering, the O^- bombardment with energy between 5 and 50 eV decreases resistivity due to the highly crystalline structure without severe damages in the film [9,10]. In spite of this progress, the final product still suffers from some physical limitations due to ionized impurities and crystallographic defects leading to resistivity currently limited at 1.0×10^{-4} Ω.cm [11,12]. In order to improve the conductivity, metal co-doping of ZnO deposited by magnetron sputtering has been proposed, as achieved in In, Ga co-doped ZnO (IGZO) [13–15] or Ga, Al co-doped ZnO (GAZO) [16–20]. Sol-gel, spray and ALD deposition methods are also used to deposit co-doped ZnO [21–26].

Nakagawara et al. [27,28] show that the disordered morphology of doped ZnO presents the best resistance to moisture. This moisture resistance is a primary request for the use of this layer in industrial applications. In their work, these authors firstly focused on Ga doped ZnO and found that the structural organization is highly disordered when exceeding 7 wt% of Ga_2O_3 content. A similar behavior was also observed for GAZO and IGZO. Indeed, the appearance of disordered GAZO is observed for Al + Ga content exceeding 8 at% [16] while for IGZO, it occurs when In + Ga exceeds 5 at% [13].

Ti, Al co-doped ZnO (TAZO) has also been proposed by Jiang and Liu [29] and Lin et al. [30,31] as a new trioxide for TCO applications in order to increase the conductivity of films thanks to the lower ionic radius of Ti^{4+} compared to Zn^{2+}. However, those studies were limited to a small range of Ti content with total Ti + Al content up to 6 at%, leading systematically to highly crystalline materials.

Moreover, the reported theoretical studies on co-doped ZnO performed at the DFT level focused principally on the substitution of Zn^{2+} by metallic element such as M^{n+} without considering interstitial

* Corresponding author.
E-mail address: Stephane.lucas@unamur.be (S. Lucas).

https://doi.org/10.1016/j.surfin.2021.101595
Received 11 July 2021; Received in revised form 25 October 2021; Accepted 7 November 2021
Available online 10 November 2021

positions and oxide formation [32,33].

Thus, the modification of the morphological, structural and opto-electronic properties of ZnO induced by Ti, Al co-doping (TAZO) is not yet fully understood. In this context, our goal is to investigate the influence of the Ti content on the properties of TAZO films for a large range of doping ratio from both an experimental and theoretical point of view.

In this study, deposition takes place by DC reactive magnetron co-sputtering of ZnAl and Ti targets at room temperature with Zn/Ti ratio as the main variable. Several Ti-doped ZnO model structures were considered at the theoretical DFT level in order to shed light on the possible structural organization within Ti-doped ZnO and the resulting changes in the electronic properties. Moreover, the influence of interstitial versus substitutional position for TiO_2 and Ti units has been investigated by the DFT calculations.

The manuscript is organized as the follows: in Section 2, materials and methods are described as well as the theoretical methodology. In Section 3, experimental results and theoretical simulations are compared and discussed. First, compositions and chemical binding energies are investigated before addressing structures and morphologies as a function of the composition. Finally, the opto-electrical properties are examined. A three-zone model attempting to rationalize the properties as a function of Ti composition is proposed at the end of Section 3. A general conclusion is presented in Section 4.

2. Materials and methods

2.1. Experimental details

Depositions were performed in an AJA orion chamber equipped with two 2″ confocal guns as sputtering sources. Process parameters are described in Table 1. O_2 reactive gas is injected in the chamber through a ring near substrates while Ar is introduced near the sputtering sources. Ar/O_2 gas flow was kept constant during all deposition processes, and both targets were operating in fully poisoned mode. Before deposition, substrates were cleaned with acetone and isopropanol during 10 min in an ultrasound bath and dried with Ar. Various substrates were used for optimal characterizations by the different techniques.

The film composition was determined on polished vitreous carbon (Neyco) by Rutherford Backscattering Spectroscopy (RBS) with alpha particles impinging the sample at normal incidence; the backscattered particles are collected at 135 ° and 165 °. Particle Induced X-ray Emission (PIXE) spectra were also recorded during RBS for complementary analysis.

X-ray Photoelectron Spectroscopy (XPS) measurements were performed on the same samples with the aim of analysing state chemical bonding of Zn and elemental composition of TAZO films. The spectrometer is an ESCALAB 250Xi (by ThermoFisher) and the Thermo Avantage software is used for analysis. The base pressure during spectra acquisition was better than 10^{-10} mbar. The excitation source was Al-Kα at 1486.6 eV equipped with a monochromator operated at 13.9 keV and 5.2 mA. The recorded spectra include Al_{2p}, C_{1s}, O_{1s}, Zn_{2p} and Zn_{LMM} and valence band and the total acquisition time was 35 min/sample. The spectra were acquired in sequential mode. The calibration and linearity of the binding energy scale are determined by $Cu_{2p3/2}$, $Ag_{3d5/2}$ and $Au_{4f7/2}$ energies. With the selected scan parameters and passing energy of 25 eV, the energy resolution was 0.7 eV compared to the FWHM of the $Ag_{3d5/2}$. The size of the analyzed sample area was 250 × 250 μm^2. A constant work function of 4.80 eV is used for all samples. The samples were stored during days in air prior to loading into the spectrometer. The transfer procedure within the spectrometer includes approximately 45 min in a parking chamber to reach a pressure of less than 10^{-7} mbar prior transfer to XPS chamber analysis. A flood gun is used to avoid charging effect. The sample surface is cleaned by cluster sputtering (Ar_{1000}, 2 keV, 120 s). Valence band spectra are referenced from Valence Band Minimum (VBM) while high-resolution spectra are referenced from adventious carbon assuming it appears at the same BE (284.8 eV [34]) for all the samples after the cluster sputtering. A K-alpha spectrometer has only been used to analyze elemental composition for the first series of sample produced in current regulation in order to compare with the composition determined by RBS. The configuration is the same as in ESCALAB 250Xi but samples are not cleaned and spot size is 400 × 400 μm^2.

Diffractograms of TAZO films deposited on soda-lime glass were collected with Cu Kα radiation (λ = 1.54184 Å) from 5 to 100 ° 2θ angle (step size of 0.0167 °) on a PANalytical X'PERT PRO Bragg-Brentano diffractometer with an X'Celerator linear detector. Tension and current of the generator were set to 45 kV and 30 mA for data collection, respectively.

Morphology of TAZO films on silicon substrate was examined by Scanning Electron Microscopy (SEM) with a JEOL 7500-F. When samples were too insulating, a thin film of gold of 10 nm was deposited to improve the conductivity.

The optical properties of the films were determined by UV–Vis-NIR spectrophotometry with a LAMBDA™ 750 spectrophotometer (Perkin Elmer) operating in transmittance mode using TAZO films deposited on soda-lime glass. LABSPHERE SRS-99–020 is used for white reference and no transmission light for black reference.

Table 1
Sputtering parameters of TAZO and ZnO: Al films. Detailed values can be found in Table S5 of Supporting Information.

Vacuum	1.0×10^{-6} Torr
Total pressure	5.8×10^{-3} Torr
Targets	Ø 2 in., Ti / Ø 2 in., ZnAl (98/2) wt%
DC Ti power/DC ZnAl power	(0–250) Watts/ (30–75) Watts
Ar flow rate	20 SCCM
O_2 flow rate	5 SCCM
Substrate temperature	Room (water-cooled)
Distance target-substrate	15.3 cm
Thickness	500–685 nm
Substrates	Glassy carbon boron doped silicon (100) soda-lime glass
Configuration	Balanced
Rotation	20 RPM

2.2. Simulations methods

Quantum-chemical calculations were performed at the density functional theory (DFT) level with periodic boundary conditions, using the 4.1 version of the SIESTA code [35,36]. The Perdew-Burke-Ernzerhof (PBE) functional was used for the description of the exchange-correlation [37]. The valence electrons were considered through a DZP (double-zeta + polarization) basis set while core electrons were described using Troullier-Martin pseudopotentials. The following valence configurations were used : O $2s^2$ $2p^4$; Ti $4s^2$ $3d^2$; Zn $4s^2$ $3d^{10}$. A mesh cut-off of 300 Ry was used with a (3 × 3 × 3) *k*-point grid. A full relaxation of the unit cell (lattice vectors and atomic positions) was achieved using the conjugated gradient scheme until the atomic forces were lower than 0.02 eV/Å. Atomic charges were computed from the relaxed electronic density using the DDEC/6 partition scheme [38].

A pristine ZnO unit cell was considered as our reference structure. From the hexagonal bulk structure, we generated an orthogonal unit cell made of 96 atoms ($Zn_{48}O_{48}$) with its *c*-axis orientated along the [000-1] direction (structures are given in Supporting Information). The size of the relaxed ZnO unit cell is $a = 10.05$ Å; $b = 11.58$ Å; $c = 10.67$.

To consider the effect of Ti-doping on the structural organization and electronic structure, we randomly introduced *n* Ti atoms (or TiO_2 units) inside the relaxed ZnO unit cell in a substitutional (S) or interstitial (I) position. The number of introduced species was chosen to generate Ti content between 1.0 and 7.0 at% ($n = 1, 2, 4, 7$ for Ti and 1, 2, 4, 8 for

TiO_2). More details about the relaxed structures for each doping ratio are given in Supporting Information (Table S1 and Section 2).

The computation of the band structure was done on the fully relaxed structures along the Γ-X-M-Γ-Y-M path using 51 k-points per band. A projected band structure and density of states (DOS) analysis were done in order to investigate the weight contribution of each atomic orbital in the DOS and band gap value.

The change in the properties of the TAZO films is expected to mainly arise from the modification of the Ti proportion since the %at of Al is constant and small (~ 2%) in each sample. Therefore, in order to keep the theoretical approach simple, the inclusion of aluminium atom was not considered in this study.

3. Results and discussion

3.1. Composition and chemical state

Fig. 1A presents the composition of the films as measured by RBS as a function of applied power ratio on Ti and ZnAl targets for samples deposited using current and power regulation. The Ti content increases from 0.0 to 17.0 at% with applied power ratio P_{Ti}/P_{ZnAl}, while the Zn content decreases from 45.5 to 20.5 at%. The oxygen content slightly increases and no significant change in Zn/Al ratio is observed. Moreover, increasing the power on the Ti target increases the relative Ti content until ~44 at% while the relative Zn and Al content decreases concomitantly.

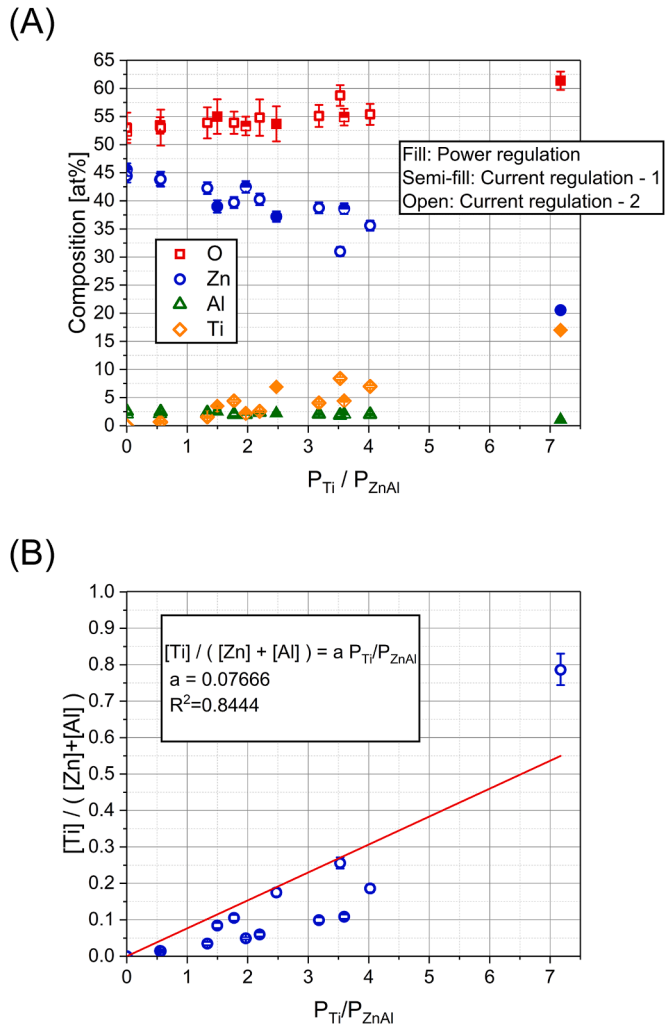

Fig. 1. (A) Composition of TAZO films measured by RBS as a function of the ratio of power applied on Ti and ZnAl targets. Filled symbols specify samples deposited using power regulation on targets while semi-filled and open symbols indicate current regulation for different series during deposition. (B) Ratio of metallic composition as a function of the ratio of powers applied; the red solid line corresponds to a fit with relation (1). The error bars are computed by taking into account the integrated alpha particle charge, the RBS cross section, and the number of detected events. (For interpretation of the references to color in this figure legend, the reader is referred to the web version of this article.)

Other sets of experiments have been done with power versus current regulation, and the film stoichiometry does not depend on the discharge regulation mode (power or current). Assuming that the Ti (Zn + Al) concentration is related to the Ti (Zn + Al) deposition rate and therefore the power applied on Ti (Zn + Al) target, one should find that:

$$\frac{[Ti]}{[Zn]+[Al]} \propto \frac{P_{Ti}}{P_{ZnAl}} \quad (1)$$

Experimental concentration-power relationship has been fitted with relation (1) as shown in Fig. 1B. At low Ti content, a slight overestimation of Ti content by relation (1) is observed. This may be due to the fact that Ti is redeposited on the ZnAl cathode during the deposition. Better process control (like OES regulated process) than just power regulation should be envisaged if one wants to control very precisely and in a reproducible way the Ti concentration in the film.

Fig. 2 presents the atomic concentration of Zn and O as a function of the atomic concentration of Ti in different unit cells of Ti-doped ZnO to be used as input for the DFT calculations, when varying the dopant position (interstitial versus substitutional) and the nature of the inserted species (Ti atom or TiO_2 unit).

Interstitial and substitutional Ti doping does not match the experimental monotonic increase in oxygen with Ti concentration as does interstitial and substitutional doping by TiO_2 units. Thus, this points to the appearance of a TiO_2 phase or a new Ti and Zn mixed oxide such as Zn_2TiO_4, as proposed by Dulin and Rase for a binary system like ZnO-TiO_2 [39].

The slight difference between Zn and O composition measured (Fig. 1A) and simulated with doping by TiO_2 unit (Fig. 2C, D) can be explained by the formation of aluminium oxide. Indeed, aluminium is expected to form Al_2O_3 due to its formation enthalpy of - 1657 kJ/mol which is very negative compared to TiO_2(- 938.57 kJ/mol) and ZnO (-350.46 kJ/mol).

The composition of TAZO films has been investigated by XPS by integration on high-resolution spectra of Ti_{2p}, Al_{2p}, O_{1s}, Zn_{2p} and Zn_{LM2} using a Shirley background. The metallic relative composition determined by XPS is similar to that determined by RBS (Table 2). Consequently, the compositions at the surface and in the bulk are very similar, pointing to a good film homogeneity.

High-resolution fit attempt for Al_{2p}, Ti_{2p}, Zn_{2p} and Zn_{LMM} of TAZO films with 10.4% of relative Ti content shows chemical binding energies corresponding to Al_2O_3 and TiO_2 (Fig. 3). However, due to numerous overlapping between binding energies of metallic oxides (TiO_2, Al_2O_3 and ZnO) on O_{1s} (Fig. S6), it is difficult to provide a quantitative realistic fit (Table S2). Moreover, the chemical shift between Zn^{2+} and Zn^0 is very small on Zn_{2p} but more pronounced on Zn_{LMM}.

Although XPS enables to study chemical binding energies, insulating films lead to a shift of the binding energies due to charge effects and hence require an accurate charge referencing. Recently, Greczynski and Hultman shows that adventitious carbon (AdC) at 284.8 eV is not the most relevant choice [40,41].

To overcome those drawbacks and determine the oxidation state of Zn, its Auger parameter (α′) is extracted. Indeed, it gives the most relevant information on the chemical environment of the zinc because it is completely independent of sample charging and of AdC referencing. This parameter is defined as [40,43,44]:

$$E_K^F\left(\mathrm{Zn}: \mathrm{L_3M_{45}M_{45}}, {}^1\mathrm{G}\right) = \alpha' - E_B^F\left(\mathrm{Zn}: 2\mathrm{p_{3/2}}\right). \quad (2)$$

It is related to the total relaxation energies (R) involved in the

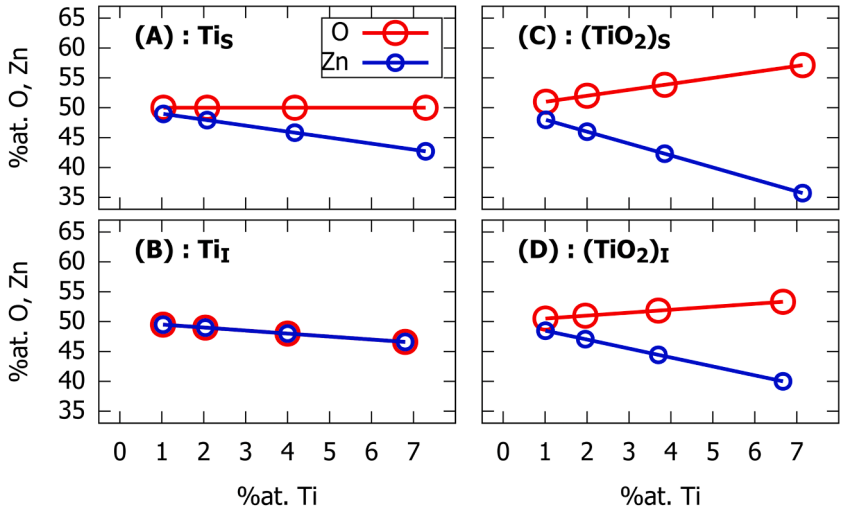

Fig. 2. Composition of zinc and oxygen inside the model unit cells as a function of the % at. of titanium for the four scenarios considered : (A) substitution of zinc atoms by titanium atoms; (B) interstition of Ti atoms inside the ZnO network; (C) substitution of zinc atoms by TiO_2 units; (D) interstition of TiO_2 units inside the ZnO network.

Table 2
TAZO film composition measured by XPS and RBS.

		Absolute composition				Relative composition Ti[%] = [Ti]/([Ti]+[Al]+[Zn])	
		RBS				RBS	XPS
	P_{Ti}/P_{ZnAl}	O [at %]	Zn [at %]	Al [at %]	Ti [at %]	Ti [%]	Ti [%]
Current regulation series 1	0.00	52.4	45.5	2.1	0.0	0.0	0.0
	0.55	53.4	43.8	2.1	0.7	1.5	1.2
	1.97	53.3	42.5	2.0	2.2	4.7	4.6
	3.59	54.9	38.6	2.1	4.4	9.8	9.5
Current regulation series 2	0.00	53.0	44.4	2.6	0.0	0.0	0.0
	0.56	53.0	43.8	2.5	0.7	1.4	2.0
	1.33	53.9	42.3	2.3	1.5	3.4	3.5
	1.77	53.9	39.7	2.0	4.4	9.6	9.8
	2.20	54.8	40.3	2.4	2.5	5.6	6.3
	3.18	55.1	38.7	2.1	4.1	9.0	10.4
	3.53	58.7	31.0	1.9	8.4	20.4	18.4
	4.02	55.4	35.6	2.0	7.0	15.7	16.2
Power regulation	1.50	55.0	39.0	2.5	3.5	7.8	6.9
	2.47	53.7	37.2	2.2	6.9	14.9	14.3
	7.17	61.4	20.5	1.1	17.0	44.0	41.5

creation of the core-hole states. The latter depicts the atomic relaxation energy relative to the core and the valence electrons and the extra-atomic relaxations and is expressed by the following relationship [43–45]:

$$\alpha' = const + 2[R^a(\text{core electrons}) + R^a(Q + \Delta Q) + R^{ea}], \quad (3)$$

where R^a(coreelectrons) is a constant independent of the chemical state, Q represents the number of valence electrons before emission of the electron R^{ea} depends of the polarizability of the environment. When no net charge transfer occurs between the environment and valence orbitals of the core-ionized atom in the final state (this is the case when s and p orbitals are involved, as it is the case for Zn), one can state that $\Delta Q = 0$ [43–45].

Generally, the Auger parameter is expressed relative to the metallic chemical state of Zn as:

$$\Delta\alpha' = \alpha'_{ZTAO} - \alpha'_{Zn} = 2\Delta R^a(Q + \Delta Q) + 2\Delta R^{ea}. \quad (4)$$

The variation of Auger parameter is shown as a function of the relative Ti content in Fig. 4A. A decrease is observed until 6.9% of Ti followed by an increase to finally stay at constant values beyond 16.2% of Ti.

The corresponding evolution of the oxidation state of Zn as a function of Ti content was also investigated at the theoretical level for the four considered approaches. The computed net atomic charge for Zn inside the pristine ZnO unit cell (+ 0.953 |e|) is considered as our reference for its + 2 oxidation state for the isolated ion. The values of the average net atomic charge of Zn atoms upon introduction of Ti atoms and TiO_2 units (in substitution or interstition) were then converted into a relative oxidation state number using this normalization. Fig. 4B presents the evolution of the Zn oxidation state with the amount of Ti content for each approach. Two trends can be distinguished (independently of the doping position): (i) a diminution of the oxidation state of Zn (i.e., pointing to a more metallic behavior) when considering the introduction of titanium into its atomic form and (ii) an increase in the oxidation state when TiO_2 units are introduced within the ZnO crystal.

Considering these results, the initial decrease in the Auger parameter (Fig. 4A) at low Ti concentration is attributed to the growing incorporation of TiO_2 units into the wurtzite ZnO network due to the increase in the oxidation state (depletion of electron density in the Zn environment) and polarizability of the chemical environment (Ti 3d orbitals). When that parameter increases back to the original value, the system switches to a situation involving probably TiO_2 clusters embedded inside ZnO, thus implying mesoscopic effects which cannot be caught by our DFT simulations. We stress that the calculated relative oxidation state is meaningful only below 4.1% at Ti (10.4% of relative Ti content) since, the Auger parameter does not evolve anymore since the Ti content measured by RBS exceeds 7.0 at% (16.2% of relative Ti content).

The valence band spectra are shown in Fig. 5 in which binding energy is set up relative to valence band maximum (VBM). Peaks at 1.6, 3.0 and 4.4 eV are mostly related to 2p orbitals of oxygen, peaks at 7.7 eV and 19.4 eV correspond respectively to Zn_{3d} and O_{2s} orbitals [47–49] while peaks at 26.4 eV and 34.3 eV are likely due to hybridized states and Ti_{3p}. When the relative Ti content increases, the peak at 3.0 eV acquires more intensity compared to those at 1.6 and 4.4 eV while the peak at 26.4 eV decreases in intensity and the Ti_{3p} contribution increases.

The decrease in the intensity of Zn_{3d} peaks is correlated to a decay of

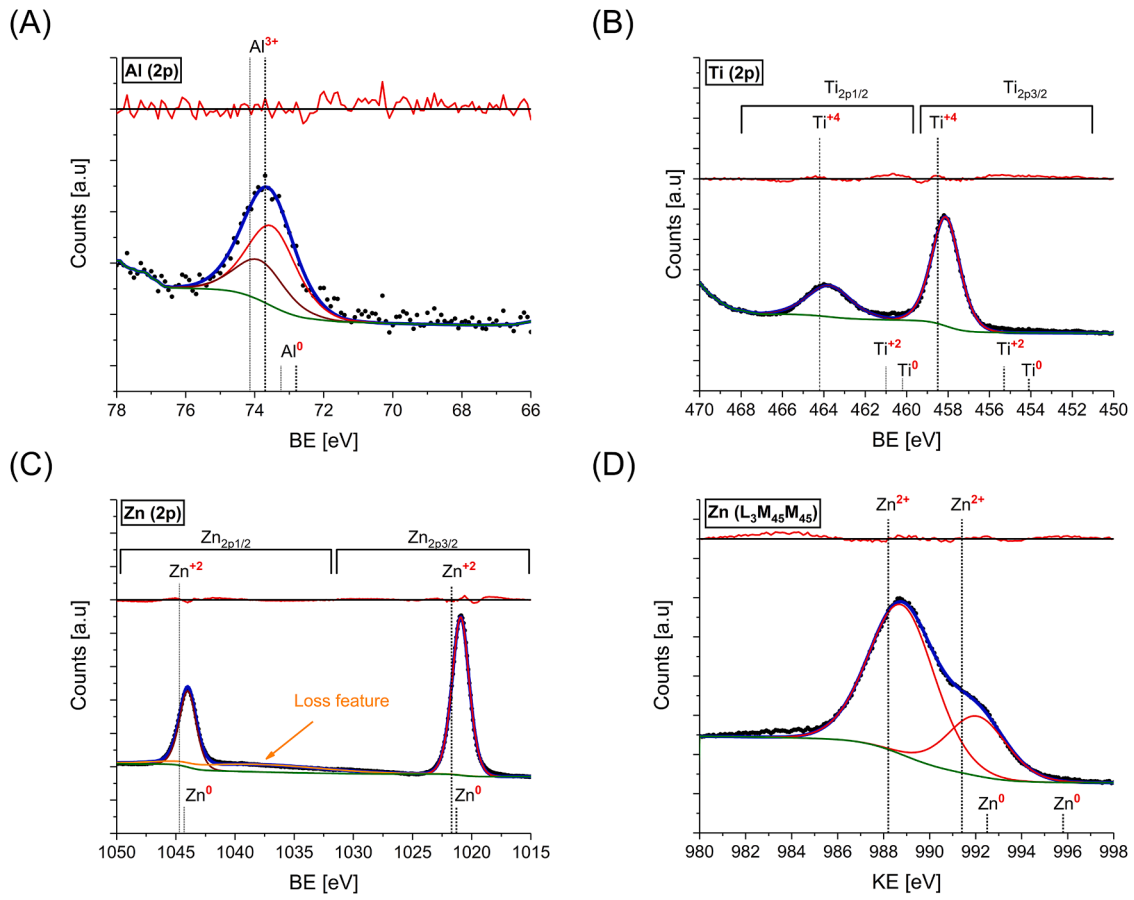

Fig. 3. High-resolution spectra for ZTAO films with 10.4% of relative Ti content for Al_{2p} (A), Ti_{2p} (B), Zn_{2p} (C) and Zn_{LMM} (D) Long vertical dot lines indicate the oxidation state of metallic elements in ZTAO films while short dot corresponds to other oxidation states [34,42].

the hybridization states. Simultaneously, the peak associated to Ti_{3p} and O_{2s} are growing as Ti content increases. Thus, the hybridization state appears to be associated to the mixing of Zn_{3d} and O_{2s} orbitals. Flattening of the O_{2p} peaks is consistent with the appearance of TiO_2 inside ZnO since the shape evolution is in good agreement with the density of states at the grain boundary calculated by Körner and Elsässer [48,50].

Altogether, the composition study suggests that Ti, Al doped ZnO is made of TiO_2 units inserted in the ZnO network at low Ti content (< 2.2 at%) doping and of mixture of TiO_2, Al_2O_3 and ZnO phases at a higher doping ratio.

Thus, only TiO_2 in substitutional or interstitial position will be studied by DFT calculations in the next sections.

3.2. Structure and morphology

Fig. 6 presents the X-ray diffraction results as a function of Ti content measured by RBS. Titanium free Al:ZnO exhibits an intense (002) peak due to a strong texturation along the c-axis perpendicular to the substrate. A small peak from (101) planes is also observed. Increasing the Ti content decreases the (002) peak that shifts toward lower diffraction angles. At the same time, the signal of the (101) orientation increases in intensity. Fig. 6B shows the ratio between the intensity of the (002) and (101) peaks. This confirms that the texturation decreases when increasing Ti content until 2.2 at% and points additionally to the amorphization of TAZO films when Ti content exceeds 7.0 at%.

Our results are consistent with literature. Indeed, a strong texturation along (002) has also been observed in previous studies on TAZO films [29–31] and other metal doped ZnO films deposited by magnetron sputtering [14,15,24]. Films grown by chemical method exhibit less texturation although a growth along (101) or (100) is also reported [21,23,25,26].

From these diffractograms, it is possible to derive the crystallite size and the stress in the films. Crystallite size is computed from the Debye-Scherrer law as:

$$g = \frac{K\lambda}{\sqrt{w^2 - L^2}\cos(\theta)}, \tag{5}$$

where K is a corrector coefficient ($K = 0.9$), λ is the Cu-Kα X-ray wavelength (λ = 0.15046nm), $w$is the Full-Width at Half-Maximum (FWHM), L is the optical instrumental error ($L = 0.0602°$) and θ is the diffraction angle.

The results presented at Fig. 6B clearly show that increasing the Ti content (from 0 to 2.2 at%) makes the crystallite size to decrease linearly. For values larger than 2.2 at%, the grain size stays constant.

This reduction of crystallite size and texturation along (002) may be explained by Al_2O_3 and TiO_2 acting as impurities in the structure zone model proposed by Barna and Adamik [51]. Indeed, TiO_2 and Al_2O_3 act as a defect in the ZnO wurtzite structure preventing the growth along (002). Similar trends have been found for Ti, H co-doped ZnO for which an excessive doping (> 6 at%) at room temperature decreases largely the crystallite size [24]. Jin et al. showed that low Ti, Al doping increases slightly the crystallite size while at higher doping ratio (> ~ 4 at%), the crystallite size decreases when the substrate is heated at 200 °C [30].

Stress parallel to the surface (σ_{film}^{XRD}) is computed from a biaxial strain model [52]. This model applied to ZnO hexagonal lattice becomes [9]:

$$\sigma_{film}^{XRD} = \frac{2C_{13}^2 - C_{33}(C_{11} + C_{12})}{2C_{13}}\varepsilon, \tag{6}$$

where ε is the strain along the c-axis.

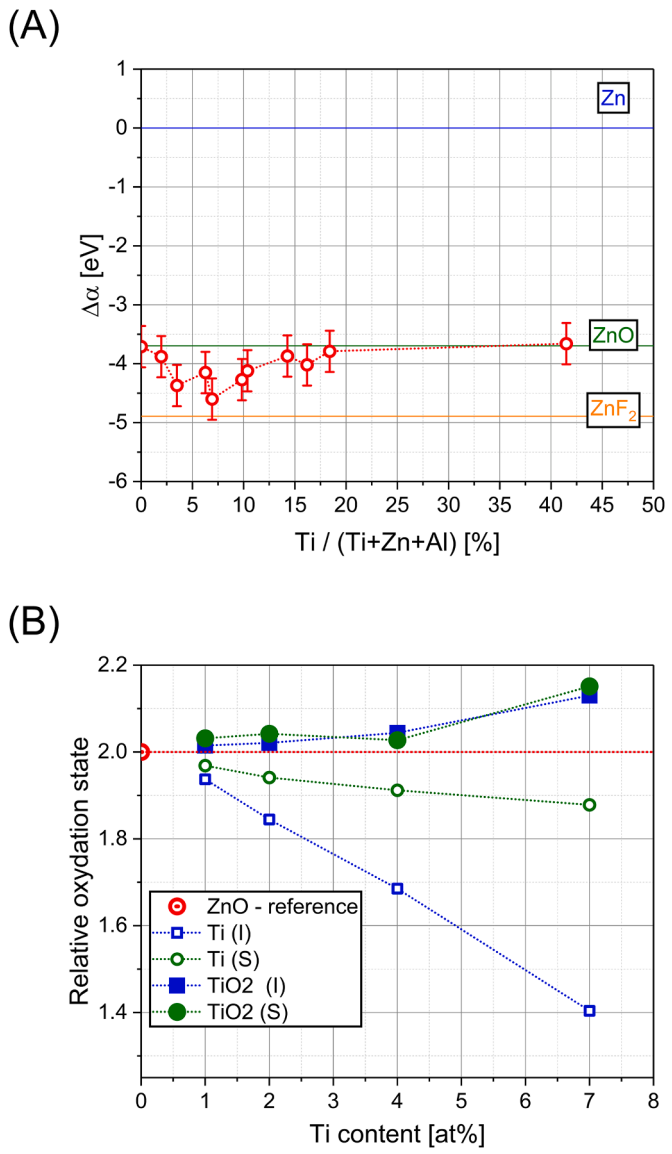

Fig. 4. (A) Auger parameter of TAZO films as a function of the relative Ti content. Auger parameters for Zn, ZnO and ZnF_2 are taken from Gaarenstroom and Winograd [46]. The error bars are estimated from the resolution in energy of the spectrometer. (B) Relative oxidation state of zinc atoms for each ZTO unit cell calculated at the DFT level by comparison to its atomic charge inside the pristine ZnO case.

$$\varepsilon = \frac{c_{film} - c_{bulk}}{c_{bulk}}, \tag{7}$$

and C_{ij} are the elastic constants (for a ZnO crystal) and $c_{bulk} = 5.2054$ Å (corresponding to 34.43 °) is the lattice parameter for the unit cell of ZnO wurtzite along the *c*-axis [53]. c_{film} is the measured lattice parameter in the deposited TAZO film. For ZnO, $C_{11} = 208.8$, $C_{33} = 213.8$, $C_{12} = 119.7$, $C_{13} = 104.2$ GPa [9].

These stress estimates can be compared with those obtained from our DFT calculations using Eq. (6). The elastic constants of ZnO were determined on the pristine $Zn_{48}O_{48}$ bulk by computing the stiffness tensor from the stress (σ)-strain (ε) proportionality relation (σ = Cε) leading to $C_{11} = 184.6$, $C_{33} = 183.5$, $C_{12} = 113.4$and$C_{13} = 99.5$ GPa [54]. The c_{bulk} and c_{film} values were extracted from our fully relaxed structures using the length of the c lattice vectors of pristine ZnO and ZTO models, respectively (Table S1). In order to determine whether the stress is either in compression or in tension, one can look at the (002) peak shift. The shift of the (002) peak toward smaller angler diffractions observed on XRD diffractograms (Fig. 6) is due to expansion along the *c*-axis of the unit cell volume of ZnO upon TiO_2 doping. This expansion results from compressive stress on TAZO films. Fig. 6C shows that the compressive stress increases linearly from - 0.7 GPa to - 8.4 GPa when Ti content increases from 0.0 at% to 7.0 at%.

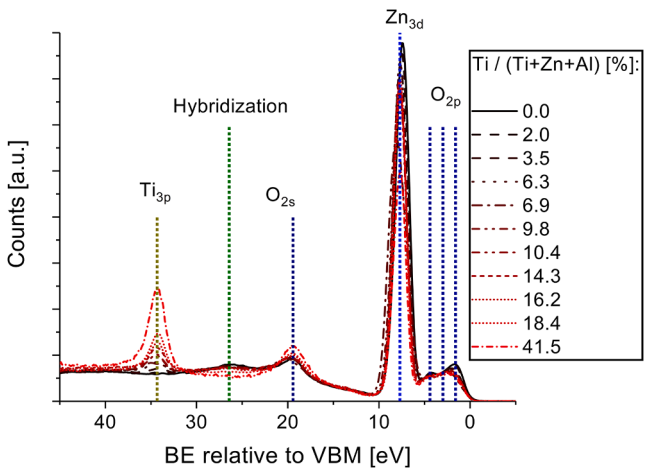

Fig. 5. Valence band spectra for TAZO films for different relative Ti contents.

The computed theoretical stress shows that TiO_2 in substitutional position gives similar slope behavior compared to the experimental data measured while TiO_2 in interstitial position gives an overestimated calculated compressive stress (larger than 10 GPa) for Ti content above 4.0 at%.

Moreover, in both doping scenarios, the introduction of TiO_2 increases the unit cell volume. The diffractograms simulated from our relaxed DFT structures (Fig. 7) confirm that the (002) peak shifts toward lower diffraction angles when an increasing number of TiO_2 units are incorporated, independently of the dopant position.

These theoretical and computational stress values suggest that TiO_2 doping occurs by substitutional doping. This will be confirmed with the optical properties, as discussed in the next section.

A similar evolution of the compressive stress has been reported by Kang et al. for GAZO films deposited by magnetron sputtering with increasing Ga/Al ratio [16]. Interestingly, a high compressive stress has also been found for films exhibiting a texturation along the a-axis, as reported by Mehmood et al. for Ti, Cu co-doped ZnO deposited by a sol-gel method [25]. This suggests that the stress is more related to the composition than the growth direction.

The surface morphology of TAZO films measured by SEM is presented in Fig. 8A–G. The increase in Ti content induces a reduction of the grain size from 51.5 ± 14.0 nm to 26.9 ± 6.0 nm, before saturating at 4.4 at%. A cauliflower shape appears when Ti exceeds 2.2 at% (Fig. 8D–F). At 17.0 at% of Ti, the cauliflower shape disappears and a morphology involving small grains appears (Fig. 8G).

TAZO films exhibit a columnar growth, as shown in cross-sectional SEM views of Fig. 8H–N. When the content exceeds 2.2 at%, the columnar growth is disturbed all over the film (Fig. 8K–M). Noteworthy, at 4.4 at% of Ti content, an inverse cone-shape appears (Fig. 8L). At high Ti content (17.0 at%), the columnar growth disappears (Fig 8N) and a more disordered film is observed without any preferential growth direction.

Similarly to the structure zone model proposed by Barna and Adamik, TAZO films evolve from a columnar morphology to an amorphous one [51]. The width of the columns decreases when the Ti content increases until 2.2 at% (Fig. 8I, J) and this occurs together with a lower *c*-axis texturation, a reduction in the crystallite size and an increase in the compressive stress (Fig. 6). Interestingly, the cauliflower shape appearing after 2.2 at% of Ti is a particular morphology which is not

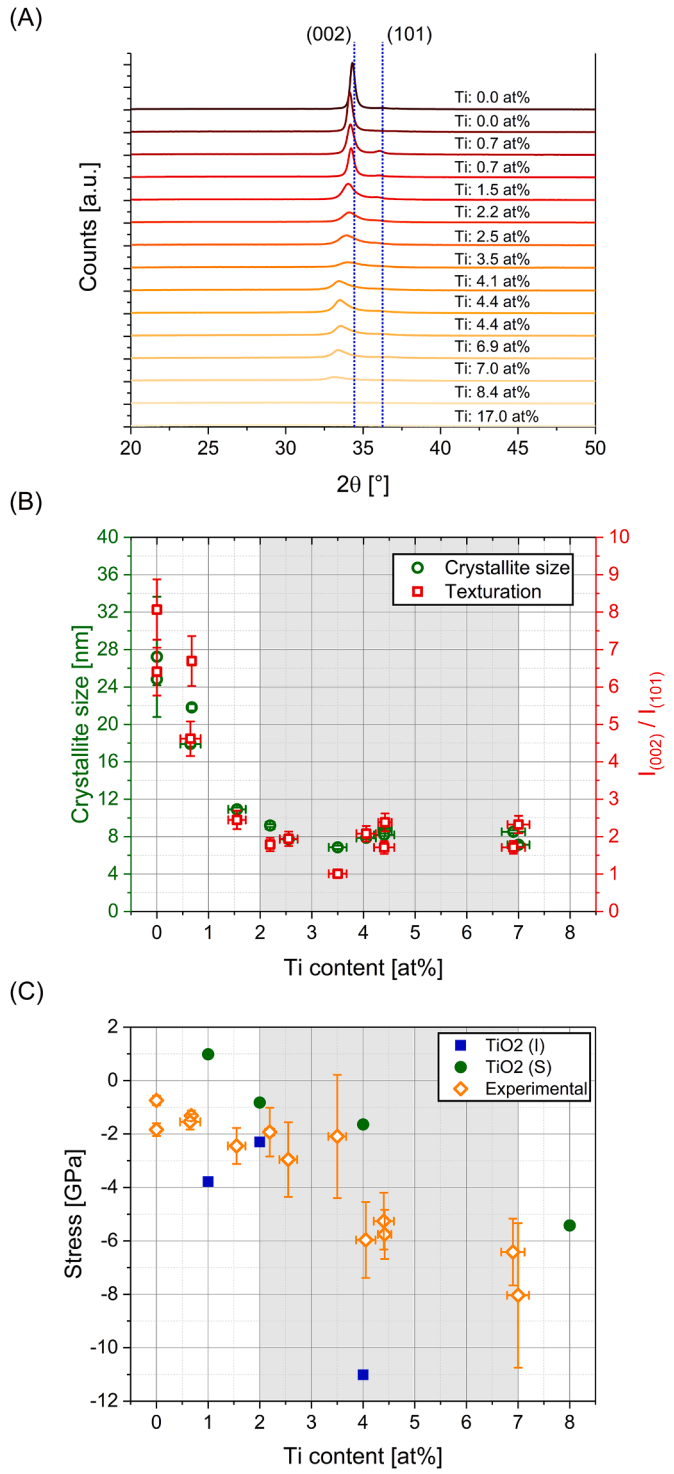

Fig. 6. (A) Diffractograms of TAZO films for different compositions of Ti content. Dot lines indicate peaks associated to the (002) and (101) planes for the ZnO wurtzite structure. (B) Intensity ratio between peaks associated to (002) and (101) and crystallite size computed from Debye-Scherrer model as a function of the Ti content in films. Error bars for the grain size are derived from Debye-Scherrer law with the error on the angle of diffraction, FWHM and peak intensity. Error bars for the texturation is derived from variations in $I_{(002)}$ and $I_{(101)}$ when different θ-ranges are used to determine the peak intensity. (C) Theoretical and experimental stress computed from a biaxial strain model applied to a hexagonal lattice. Error bars for the stress are computed by taking into account the error on the angle of diffraction of the (002) peak in the strain measurement by Bragg's law.

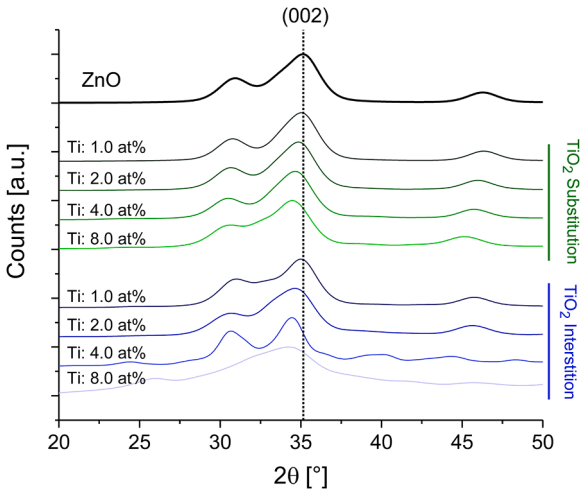

Fig. 7. Simulated X-ray diffractogram for ZnO doped with TiO_2 units in substitutional and interstitial position as a function of Ti composition.

explained by the structure zone model of Barna and Adamik. One hypothesis is that a large stress pushes up crystallites out of the films, as observed in Fig. 8L. If one looks at the top SEM view in Fig. 8D–F, it is seen that the cauliflower structure is present as long as the coatings are crystalline (grey area on Fig. 6B, C). For Ti content > 7.0 at%, this particular feature is not anymore observed and films become amorphous with a random orientation growth, as predicted by the structure zone model of Barna and Adamik [51]. Noteworthy, this inverse cone-shape feature appears at the minimum value of the Auger parameter (2009.24 eV) and disappears when the Auger parameter increases, which indicates that this particular shape is probably related to more oxidized states of Zn.

3.3. Optical and electrical properties

Attempts to measure the surface resistivity of the samples with a four-point method (Van der Pauw and linear configurations) failed, implying that all the samples are largely insulating. This could be due to the formation of a highly resistive Al_2O_3 secondary phase coming from the sputtering of the Zn/Al target. According to Sieber et al. [55], this additional phase is generally formed at the grain boundaries.

Optical transmission spectra measured between 250 and 2500 nm are shown Fig. 9A. All the curves look similar, with a high transmittance in the visible and infrared range. A closer analysis shows that increasing Ti content shifts the transmittance shoulder towards lower wavelengths. The transmittance in the visible range increases until 2.5 at% of Ti and stays in the typical range of [82.5; 85.0]% for larger Ti content until 8.4 at%, as shown in Fig. 9B. The average transmittance in the visible (between 380 and 780 nm) and near infrared (780 and 2500 nm) gradually decreases beyond this concentration.

The band structures and projected density of states (PDOS) have been computed for pristine ZnO (Fig. 10A), Ti-doped ZnO with 1 and 8 TiO_2 units in interstitial (Fig. 10B, C) or substitutional (Fig. 10D, E) position. The band structure of the pristine wurtzite ZnO phase is already well described in literature and shows a direct band gap at the Γ point [56]. The value of the energy gap computed at the GGA-PBE level amounts to 0.84 eV and is fully consistent with other reported DFT works [57–59]. This value is very small compared to the experimental value measured for the pure ZnO wurtzite phase (3.27 eV); this is a well-known effect when using LDA or GGA functionals to describe the fundamental gap of semiconductors [60]. This effect is even worse for ZnO and results from an upshift of the valence band due to Zn_{3d}/O_{2p} electron repulsion [61]. However, this is not a severe issue here since the nature of the band states is reliably described and we are mainly

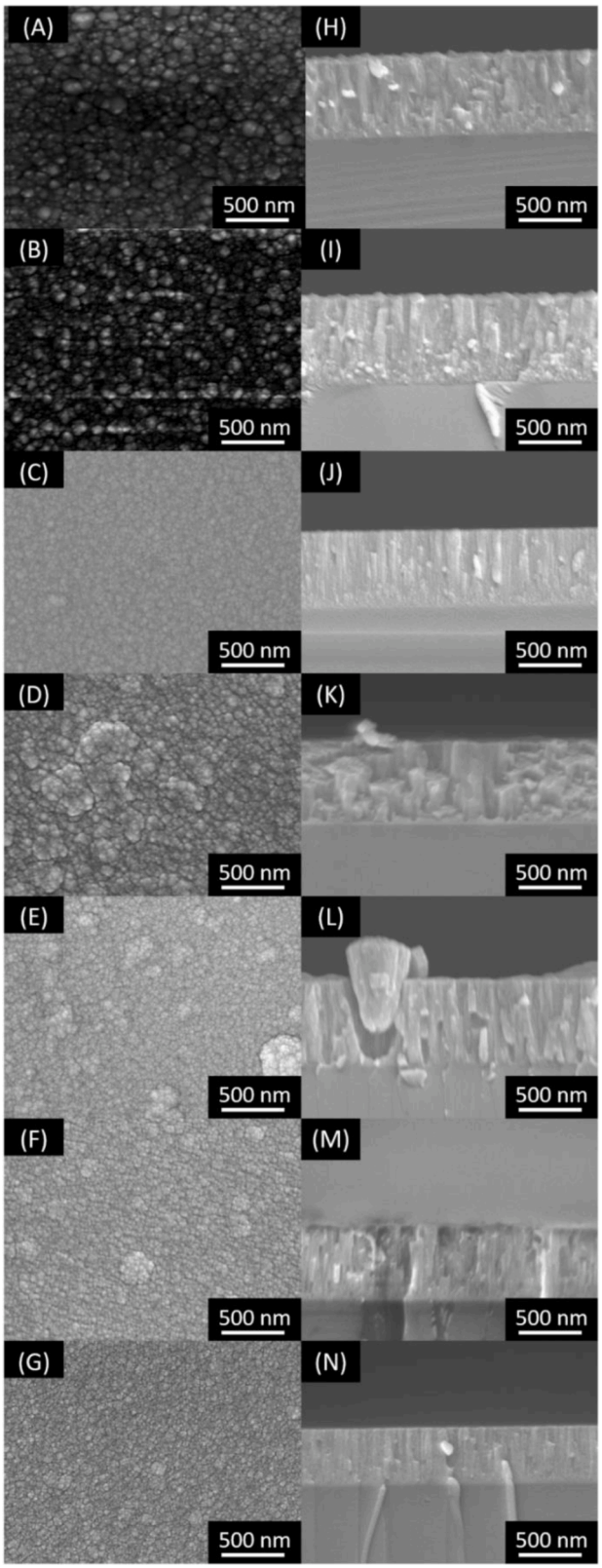

Fig. 8. (Left) TAZO films surface captured for (A) 0 at%,(B) 0.7 at%, (C) 2.2 at %, (D) 3.5 at%, (E) 4.4 at%, (F) 6.9 at% and (G) 17.0 at% of Ti content; (Right) corresponding TAZO films cross-sections.

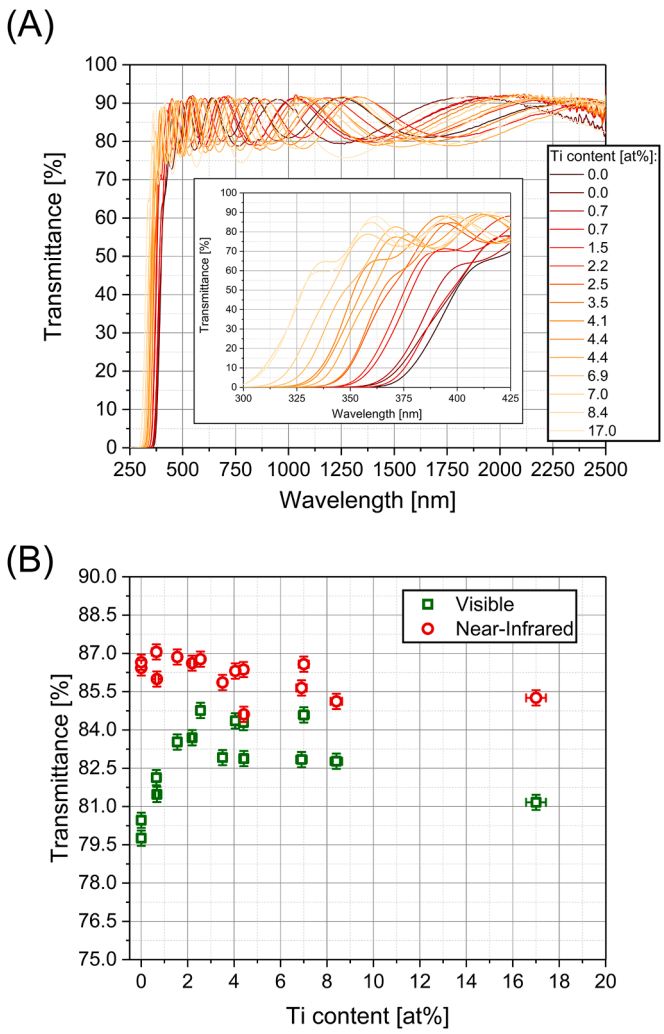

Fig. 9. (A) Transmittance spectra of ZnO: TiAl films for different Ti contents. (B) Average transmittance in function of Ti content for visible and near-infrared. Error bars represent the noise of the spectrophotometer.

concerned by the relative changes in the oxide band gap when increasing the amount of titanium atoms. The band structure calculated for 1 and 8 TiO_2 in interstitial or substitutional position supports the fact that the Zn_{4s}/Ti_{3d} hybridization in ZnO doped by TiO_2 units opens the bandgap of pristine ZnO.

In order to a better comparison between the experimental and theoretical data, we applied an arbitrary offset of 2.43 eV to the computed band gap, hence fixing the DFT value of ZnO to its experimental value of 3.27 eV.

From transmittance spectra, the electronic gap can be estimated using Tauc formula [62,63],

$$(\alpha h\nu)^{\frac{1}{n}} = h\nu - E_g, \tag{8}$$

where the absorption coefficient α(λ) is linked to $T(\lambda)$ by the approximated equation:

$$\alpha(\lambda) = \left(\frac{1}{d}\right)\ln\left(\frac{1}{T^2(\lambda)}\right), \tag{9}$$

where d is the film thickness, $T(\lambda)$ is the transmittance spectrum, λ is the wavelength, ν is the associated frequency, h is the Bolztmann constant, E_g is the gap and n is a coefficient equal to ½ for a semiconductor with a direct gap, as it is the case for TAZO films.

The experimental shift of transmittance edge reflects a

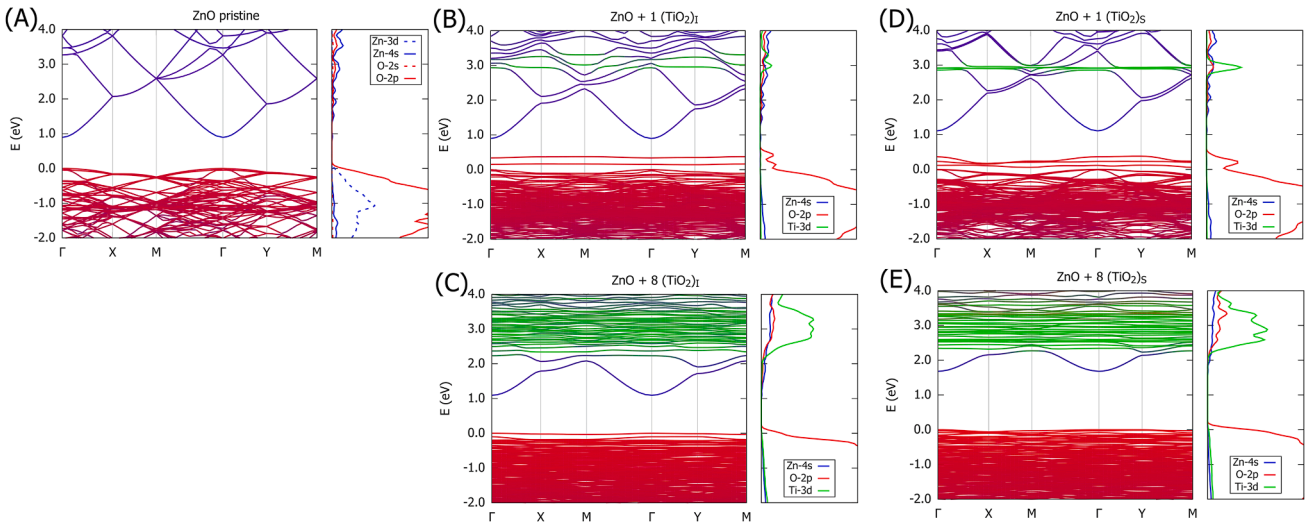

Fig. 10. Band structures and projected density of states (PDOS) of (A) pristine ZnO; (B) ZnO + 1 TiO_2 in interstitial position; (C) ZnO + 8 TiO_2 in interstitial position; (D) ZnO + 1 TiO_2 in substitutional position; (E) ZnO + 8 TiO_2 in substitutional position. The band structures are coloured as a function of the atomic orbital contribution: red (O orbitals), blue (Zn orbitals), green (Ti orbitals). (For interpretation of the references to color in this figure legend, the reader is referred to the web version of this article.)

corresponding shift in the gap, and hence in the absorption edge.

The evolution of the experimental bandgap and simulated electronic gap as a function of the Ti content is shown in Fig. 11. The gap derived by the Tauc formula increases with Ti content until 8.4 at% and stays constant beyond. The unexpected decrease in bandgap with a Ti content exceeding 0.59 at% observed by Lin et al. [30] is not detected in our case but reproduces the increase in the bandgap when adding a small amount of Ti reported in a previous study [29].

The linear increase in the bandgap with the amount of Ti is in excellent agreement with the simulations when considering a substitution of Zn atoms by TiO_2 units, while TiO_2 in interstitial position leads to a smaller opening of the energy gap. Altogether, these results support the fact that additional titanium atoms are inserted in the zinc oxide in their 5 or 6-fold coordinated form (such as in TiO_2); nevertheless, we cannot exclude the formation of separated ZnO/TiO_2 domains at Ti

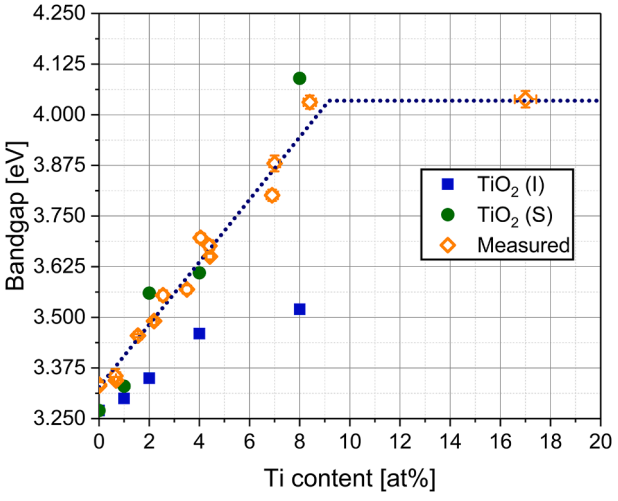

Fig. 11. Evolution of the bandgap as a function of Ti composition from the computed band-structures after renormalization for TiO_2 units in interstitial (blue square) and substitutional (green circle) position. Experimental bandgaps computed from Tauc plot (orange diamond). Error bars are estimated by propagating the error over the average of three measurements of bandgap by Tauc plots. (For interpretation of the references to color in this figure legend, the reader is referred to the web version of this article.)

content exceeding 7.0 at%.

Similarly, works on Ga, Al co-doped ZnO show an increase in the bandgap with an increase of Ga and Al content due to occupied Al_{3s} and Ga_{4s} lying at the bottom of the conduction band and raising up the Fermi level up to the conduction band edge [21,33]. This effect is depicted as a Burstein-Moss effect and leads to an increase in the charge carrier concentration in the coatings and hence in the conductivity [64,65]. A similar phenomenon was also demonstrated when substituting oxygen by fluorine in Al, F co-doped ZnO (AFZO) [23].

On the other side, Cu, Al co-doped ZnO has been also explored by DFT and results show that Cu^{2+} reduced the bandgap due to hybridization between Cu_{3d} orbitals and O_{2p} and by generation of impurity levels in the bandgap by Cu_{3d}. Moreover, Cu doped ZnO does not exhibit a significant modification of the Fermi level [32]. This points principally that hybridization of d-orbitals (with O_{2p} in the valence band or Zn_{4s} in the conduction band) is another mechanism tailoring the bandgap which does not lead necessarily to a conducting material.

The fact that TAZO films are not conducting films support the fact that, in this case, the increase in bandgap is due to hybridization between Ti_{3d} and Zn_{4s} orbitals.

3.4. Zone model

Fig. 12 summarizes our findings for the formation of Ti, Al co-doped ZnO. Three zones are involved, and all of them includes the formation of Al_2O_3 leading to the insulating character of the films as shown by XPS analysis Fig. 3A.

Zone I describes the situation for Ti $\leq$ 2.2 at%. In this regime, TiO_2 units substitute Zn atoms in the ZnO wurtzite structure, as supported by the fact that the Auger parameter decreases with Ti content, confirming that the zinc atoms are in a more oxidized state upon introduction of substitutional TiO_2 units in ZnO wurtzite (Fig. 4). Crystallites of ZnO growth preferentially along the c-axis giving rise to textured films (Fig. 6A). Grain and crystallite sizes as well as texturation decrease linearly with the Ti content until 2.2 at% (Fig. 6B). TiO_2 doping induces low compressive stress (less than 4.0 GPa) as shown in Fig. 6C. Columnar growth is observed and width of the columns decreases (Fig. 8H–J). This part of the model is similar to Zone T in the structure zone model of Barna and Adamik [51]. Hybridization between Zn_{4s} and Ti_{3d} orbitals in the conduction band leads to an increase in the bandgap (Fig. 10B) which is paralleled by an increase in the transmittance in the visible

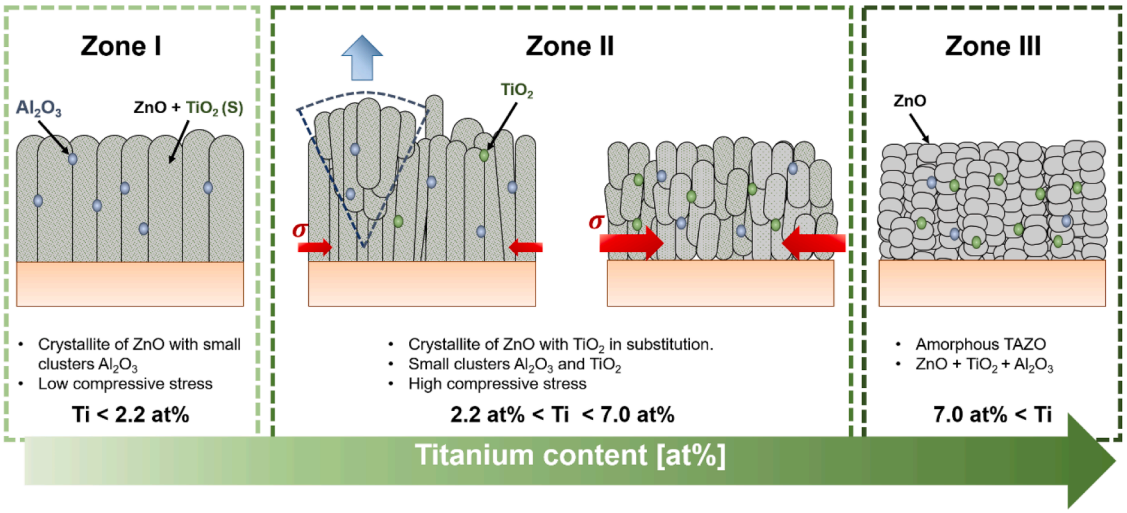

Fig. 12. Schematic growth of TAZO films with growing Ti content. Blue: Al_2O_3, green: TiO_2. Zone I is a crystalline zone at low Ti content. Zone II is a transition zone between crystalline and amorphous phases in which the Ti content strongly influences the structure and morphology. Zone III is an amorphous zone where the Ti content has completely change the morphology and structure of the film. (For interpretation of the references to color in this figure legend, the reader is referred to the web version of this article.)

range with the Ti content (Fig. 9B). In this regime, all experimental results are well supported by DFT simulations.

In Zone II (2.2 at.% < Ti ≤ 7.0 at.%), the TiO_2 units continue to substitute Zn atoms with the formation of small clusters of TiO_2 as revealed by the increase in the Auger parameter indicating that Zn regains its chemical state in pristine ZnO (Fig. 4) while the chemical state of Ti is unchanged (Fig. S7). TAZO films are in a transition regime between a fully crystalline and amorphous film as shown by diffractograms (Fig. 6A). Grain and crystallite size do not decrease anymore and films are less texturated (Fig. 6B). The increase in Ti content induces high internal compressive stress (more than 4.0 GPa) as exhibited in Fig. 6C. At this stage, columnar ZnO are pushed up forming a particular cauliflower shape, as shown Fig. 8L. The bandgap keeps increasing due to hybridization between Ti_{3d} and Zn_{4s} as shown Fig. 10**C.**

Finally, in Zone III (Ti > 7.0 at%), Zn has completely regained its initial chemical state of ZnO (Fig. 4) and it is assumed that the film is made of ZnO with TiO_2 and Al_2O_3 forming small clusters segregated at grain boundaries. TAZO films are amorphous as shown in Fig. 6A and show random orientation of growth (Fig. 8N). This part of the zone is similar to the structure zone model proposed by Barna and Adamik [51]. For this regime, the bandgap is constant (Fig. 11) and DFT simulations are unable to depict the mesoscopic/macroscopic effect of formation of TiO_2 and Al_2O_3 clusters.

4. Conclusions

The morphology, structure and electronic properties of Ti, Al co-doped ZnO thin films deposited by reactive magnetron sputtering have been studied as a function of Ti content. The content in Ti follows a law depending on the power applied on targets, as expected from laws governing plasma depositions.

The substitutional and interstitial position of Ti and TiO_2 units has been studied by DFT; this systematic and comparative study has never been reported previously to the best of our knowledge. It has been shown experimentally and supported by DFT simulations that TiO_2 substitutes Zn in TAZO films. Film growth takes place by the incorporation of TiO_2 in a ZnO network with all resulting properties governed by the quantity of Ti incorporated.

TAZO are insulating films under the present experimental conditions, probably due to the presence of Al_2O_3 at grain boundaries. The deposition of conducting films is expected by substrate heating during deposition, as evidenced by Lin et al. [30,31]. Addressing the role of substrate temperature is beyond the scope of the present paper but clearly deserves a major attention.

The major findings are wrapped up into a three-zone model proposed to depict the general morphological/optical behavior of Ti, Al co-doped ZnO with the Ti content. At small Ti content (Ti < 2.2 at%), Ti is incorporated as substitutional TiO_2 in the TAZO films with structure and morphology close to Al doped ZnO, i.e., with a high texturation along the *c*-axis and a columnar growth such as proposed by Barna and Adamik in its structure zone model [51]. Optical properties are explained by hybridization between Ti_{3d} and Zn_{4s} orbitals In this regime, the experimental data are fully supported by our DFT calculations.

At intermediate content (2.2 at% < Ti < 7.0 at%), substitution leads to small TiO_2 clusters. TiO_2 increases the compressive stress, generating first a cauliflower shape based morphology and next a more disordered columnar growth. This cauliflower shape has never been encountered within magnetron sputtering. The bandgap continues to increase due to hybridization between Ti_{3d} and Zn_{4s} orbitals.

Although some TiO_2 clusters can be observed in our simulations for unit cells containing ~ 7.0 at%, this clustering was not fully investigated in our simulations due to the small size of the unit cell considered for the DFT approach (typical length of ~10 Å). The formation of these clusters appears as a mesoscopic effect, as confirmed by the data at higher doping ratio.

Indeed, a further increase in TiO_2 (Ti exceeding 7.0 at%) causes random orientation of growth and amorphization of TAZO films. TiO_2 and Al_2O_3 clusters thus appear as impurities in the structure zone model proposed by Barna and Adamik [51].

Associated contents

Supporting informations include a table of structural parameters of the relaxed unit cells of pristine ZnO and Ti/ TiO_2 units in interstional/ substitutional doping position in ZnO wurtzite structure. Side view of these fully relaxed units cells are shown. High resolution spectra of Zn_{2p}, Ti_{2p}, Al_{2p}, C_{1s}, O_{1s} photoemitted electrons and Zn_{LM2} Auger electrons after surface cleaning by cluster sputtering (Ar_{1000}, 2 keV, 120 s) are shown for different Ti content (pdf).

CRediT authorship contribution statement

Florian Bocchese: Investigation, Writing – original draft, Formal analysis, Writing – review & editing. **David Cornil:** Formal analysis,

Writing – review & editing. **Emile Haye:** Writing – review & editing. **Jérôme Cornil:** Writing – review & editing, Funding acquisition. **Stéphane Lucas:** Funding acquisition, Conceptualization, Writing – review & editing.

Declaration of Competing Interest

The authors declare that they have no known competing financial interests or personal relationships that could have appeared to influence the work reported in this paper.

Acknowledgments

The Synthesis Irradiation and Analysis of Materials (SIAM), PC^2, MORPH-IM and LOS platforms of UNamur are acknowledged for XPS, RBS, XRD, UV-Vis-NIR and SEM measurements. Authors would like particularly thank to Julien Colaux for his help during RBS measurements. The DFT calculations were supported by the Consortium des Équipements de Calcul Intensif (CÉCI), funded by the Fonds National de la Recherche Scientifique (F. R. S.-FNRS) under Grant No. 2.5020.11. J. C. is an FNRS Research Director. The research in Mons is also supported by AGC Glass Europe and the Walloon region; the research in Namur is also supported by AGC Glass Europe.

Supplementary materials

Supplementary material associated with this article can be found, in the online version, at doi:10.1016/j.surfin.2021.101595.

References

[1] K. Nomura, H. Ohta, A. Takagi, T. Kamiya, M. Hirano, H. Hosono, Room-temperature fabrication of transparent flexible thin-film transistors using amorphous oxide semiconductors, Nature 432 (2004) 488–492, https://doi.org/10.1038/nature03090.

[2] H.Q. Chiang, J.F. Wager, R.L. Hoffman, J. Jeong, D.A. Keszler, High mobility transparent thin-film transistors with amorphous zinc tin oxide channel layer, Appl. Phys. Lett. (2005), 013503, https://doi.org/10.1063/1.1843286.

[3] H. Yabuta, M. Sano, K. Abe, T. Aiba, T. Den, H. Kumomi, K. Nomura, T. Kamiya, H. Hosono, High-mobility thin-film transistor with amorphous $InGaZnO_4$ channel fabricated by room temperature RF-magnetron sputtering, Appl. Phys. Lett. (2006), 112123, https://doi.org/10.1063/1.2353811.

[4] C.G. Granqvist, Transparent conductors as solar energy materials : a panoramic review, Sol. Energy Mater. Sol. Cells 91 (2007) 1529–1598, https://doi.org/10.1016/j.solmat.2007.04.031.

[5] D.R. Sahu, S. Lin, J. Huang, ZnO/Ag/ZnO multilayer films for the application of a very low resistance transparent electrode, Appl. Surf. Sci. 252 (2006) 7509–7514, https://doi.org/10.1016/j.apsusc.2005.09.021.

[6] D.R. Sahu, J. Huang, High quality transparent conductive ZnO/Ag/ZnO multilayer films deposited at room temperature, Thin Solid Films 515 (2006) 876–879, https://doi.org/10.1016/j.tsf.2006.07.049.

[7] D.R. Sahu, C.Y. Chen, S.Y. Lin, J. Huang, Effect of substrate temperature and annealing treatment on the electrical and optical properties of silver-based multilayer coating electrodes, Thin Solid Films 515 (2006) 932–935, https://doi.org/10.1016/j.tsf.2006.07.061.

[8] T. Minami, New *n*-type transparent conducting oxides, MRS Bull. 25 (8) (2000) 38–44, https://doi.org/10.1557/mrs2000.149.

[9] R. Cebulla, R. Wendt, K. Ellmer, Al-doped zinc oxide films deposited by simultaneous RF and DC excitation of a magnetron plasma: relationships between plasma parameters and structural and electrical film properties, J. Appl. Phys. 83 (1998) 1087–1095, https://doi.org/10.1063/1.366798.

[10] K. Ellmer, Magnetron sputtering of transparent conductive zinc oxide: relation between the sputtering parameters and the electronic properties, J. Phys. D Appl. Phys. (2000) 33, https://doi.org/10.1088/0022-3727/33/4/201.

[11] K. Ellmer, Past achievements and future challenges in the development of optically transparent electrodes, Nat. Photon. 6 (2012) 809–817, https://doi.org/10.1038/NPHOTON.2012.282.

[12] K. Ellmer, Resistivity of polycrystalline zinc oxide films : current status and physical limit, J. Phys. D Appl. Phys. 34 (2001) 3097–3108, https://doi.org/10.1088/0022-3727/34/21/301.

[13] D.P. Pham, H.T. Nguyen, B.T. Phan, T.M.D. Cao, V.D. Hoang, V.A. Dao, J. Yi, C. V. Tran, In and Ga co doped ZnO film as a front electrode for thin film silicon solar cells, Adv. Condens. Matter Phys. 2014 (2014) 1–7, https://doi.org/10.1155/2014/971528.

[14] D.P. Pham, H.T. Nguyen, B.T. Phan, V.D. Hoang, S. Maenosono, C.V. Tran, Influence of addition of indium and of post-annealing on structural, electrical and optical properties of gallium-doped zinc oxide thin films deposited by direct-current magnetron sputtering, Thin Solid Films 583 (2015) 201–204, https://doi.org/10.1016/j.tsf.2015.03.068.

[15] N.H. Tran Nguyen, T.H. Nguyen, Y.R. Liu, M. Aminzare, A.T.T. Pham, S. Cho, D. P. Wong, K.H. Chen, T. Seetawan, N.K. Pham, H.K.T. Ta, V.C. Tran, T.B. Phan, Thermoelectric properties of indium and gallium dually doped ZnO thin films, ACS Appl. Mater. Interfaces 8 (2016) 33916–33923, https://doi.org/10.1021/acsami.6b10591.

[16] D.W. Kang, S.J. Kim, T.H. Moon, H.M. Lee, M.K. Han, Effect of Ga doping on transparent and conductive Al-doped ZnO films prepared using magnetron cosputtering, Jpn. J. Appl. Phys. (2010) 49, https://doi.org/10.1143/JJAP.49.125801.

[17] C.A. Gupta, S. Mangal, U.P. Singh, Impact of sputtering power on the properties of Al and Ga co-sputtered ZnO thin films, J. Mater. Sci. Mater. Electron. 26 (2015) 4280–4284, https://doi.org/10.1007/s10854-015-2979-2.

[18] K. Zhu, Y. Yang, W. Song, Effects of substrate temperature on the structural, morphological, electrical and optical properties of Al and Ga co-doped ZnO thin films grown by DC magnetron sputtering, Mater. Lett. 145 (2015) 279–282, https://doi.org/10.1016/j.matlet.2015.01.130.

[19] S.K. Sahoo, C.A. Gupta, U.P. Singh, Impact of Al and Ga co-doping with different proportion in ZnO thin film by DC magnetron sputtering, J. Mater. Sci. Mater. Electron. 27 (2016) 7161–7166, https://doi.org/10.1007/s10854-016-4679-y.

[20] C. Lung, M. Toma, M. Pop, D. Marconi, A. Pop, Characterization of the structural and optical properties of ZnO thin films doped with Ga, Al and (Al+Ga), J. Alloys Compd. 725 (2017) 1238–1243, https://doi.org/10.1016/j.jallcom.2017.07.265.

[21] R. Ebrahimifard, M.R. Golobostanfard, H. Abdizadeh, Sol-gel derived Al and Ga co-doped ZnO thin films: an optoelectronic study, Appl. Surf. Sci. 290 (2014) 252–259, https://doi.org/10.1016/j.apsusc.2013.11.062.

[22] N. Guermat, W. Daranfed, I. Bouchama, N. Bouarissa, Investigation of structural, morphological, optical and electrical properties of Co/Ni co-doped ZnO thin films, J. Mol. Struct. 1225 (2021), 129134, https://doi.org/10.1016/j.molstruc.2020.129134.

[23] K.M. Kang, Y. Wang, M. Kim, C. Lee, H.H. Park, Al/F codoping effect on the structural, electrical, and optical properties of ZnO films grown via atomic layer deposition, Appl. Surf. Sci. 535 (2021), 147734, https://doi.org/10.1016/j.apsusc.2020.147734.

[24] F.H. Wang, J.C. Chao, H.W. Liu, T.K. Kang, Physical properties of ZnO thin films co doped with titanium and hydrogen prepared by RF magnetron sputtering with different substrate temperatures, J. Nanomater. (2015), https://doi.org/10.1155/2015/936482, 2015.

[25] B. Mehmood, M.I. Khan, M. Iqbal, A. Mahmood, W. Al-Masry, Structural and optical properties of Ti and Cu co-doped ZnO thin films for photovoltaic applications of dye sensitized solar cells, Int. J. Energy Res. 45 (2021) 2445–2459, https://doi.org/10.1002/er.5939.

[26] A. Das, P. Guha Roy, A. Dutta, S. Sen, P. Pramanik, D. Das, A. Banerjee, A. Bhattacharyya, Mg and Al co-doping of ZnO thin films: effect on ultraviolet photoconductivity, Mater. Sci. Semicond. Process. 54 (2016) 36–41, https://doi.org/10.1016/j.mssp.2016.06.018.

[27] Nakagawara O., Seto H., Kishimoto Y., Murata Manufacturing Co Ltd. *Transparent conductive film and method for manufacturing the same.* (2011) US7867636B2.

[28] O. Nakagawara, Y. Kishimoto, H. Seto, Y. Koshido, Y. Yoshino, T. Makino, Moisture-resistant ZnO transparent conductive films with Ga heavy doping, Appl. Phys. Lett. 89 (2006) 1–4, https://doi.org/10.1063/1.2337542.

[29] M. Jiang, X. Liu, Structural, electrical and optical properties of Al-Ti co doped ZnO (ZATO) thin films prepared by RF magnetron sputtering, Appl. Surf. Sci. 255 (2008) 3175–3178, https://doi.org/10.1016/j.apsusc.2006.11.032.

[30] J. Lin, J.N. Wu, C.A. Tseng, K.C. Peng, Effect of direct current power to Ti-target on the composition, structure and characterization of the Ti (0–2.36 at.%), Al codoped ZnO sputtering thin films, Jpn. J. Appl. Phys. 52 (2013) 52, https://doi.org/10.7567/JJAP.52.01AC06.

[31] J. Lin, M. Huang, T. Wang, J. Wu, Y. Tseng, K.C. Peng, Structure and characterization of the sputtered ZnO, Al-doped ZnO, Ti-doped ZnO and Ti, Al-co-doped ZnO thin film, Mater. Express 5 (2015) 153–158, https://doi.org/10.1166/mex.2015.1218.

[32] J. Dai, Z. Suo, Z. Li, S. Gao, Effect of Cu/Al doping on electronic structure and optical properties of ZnO, Res. Phys. 15 (2019), 102649, https://doi.org/10.1016/j.rinp.2019.102649.

[33] M. Khuili, G. El Hallani, N. Fazouan, H.A. El Makarim, E.H. Atmani, First-principles calculation of (Al, Ga) co-doped ZnO, Comput. Condens. Matter 21 (2019) e00426, https://doi.org/10.1016/j.cocom.2019.e00426.

[34] J.F. Moulder, W.F. Stickle, P.E. Sobol, K.D. Bomben, Handbook of X-Ray Photoelectron Spectroscopy, Perkin-Elmer Corporation, 1992.

[35] J.M. Soler, E. Artacho, J.D. Gale, A. Garcia, J. Junquera, P. Ordejon, D. Sanchez-Portal, The SIESTA method for *ab initio* order-N materials simulation, J. Phys. Condens. Matter 14 (2002) 2745, https://doi.org/10.1088/0953-8984/14/11/302.

[36] E. Artacho, E. Anglada, O. Diéguez, J.D. Gale, a García, J. Junquera, R.M. Martin, P. Ordejón, J.M. Pruneda, D. Sánchez-Portal, J.M. Soler, The SIESTA method: developments and applicability, J. Phys. Condens. Matter 20 (2008), 064208, https://doi.org/10.1088/0953-8984/20/6/064208.

[37] J.P. Perdew, K. Burke, M. Ernzerhof, Generalized gradient approximation made simple, Phys. Rev. Lett. 77 (1996) 3865–3868, https://doi.org/10.1103/PhysRevLett.77.3865.

[38] T.A. Manz, N.G. Limas, Introducing DDEC6 atomic population analysis: part 1. Charge partitioning theory and methodology, RSC Adv. 6 (2016) 47771–47801, https://doi.org/10.1039/c6ra04656h.

[39] F.H. Dulin, D.E. Rase, Phase equilibria in the system ZnO-TiO_2, J. Am. Ceram. Soc. 43 (1960) 125–131, https://doi.org/10.1111/j.1151-2916.1960.tb14326.x.
[40] G. Greczynski, L. Hultman, Progress in materials science X-ray photoelectron spectroscopy : towards reliable binding energy referencing, Prog. Mater. Sci. 107 (2020), 100591, https://doi.org/10.1016/j.pmatsci.2019.100591.
[41] G. Greczynski, L. Hultman, Compromising science by ignorant instrument calibration -need to revisit half a century of published XPS data, Angew. Chem. 59 (2020) 5002–5006, https://doi.org/10.1002/anie.201916000.
[42] G. Schön, Auger and direct electron spectra in X-ray photoelectron studies of zinc, zinc oxide, gallium and gallium oxide, J. Electron Spectrosc. Relat. Phenom. 2 (1973) 75–86, https://doi.org/10.1016/0368-2048(73)80049-0.
[43] G. Moretti, Auger parameter and Wagner plot in the characterization of chemical states by X-ray photoelectron spectroscopy : a review, J. Electron Spectrosc. Relat. Phenom. 95 (1998) 95–144, https://doi.org/10.1016/S0368-2048(98)00249-7.
[44] G. Moretti, The Wagner plot and the Auger parameter as tools to separate initial- and final-state contributions in X-ray photoemission spectroscopy, Surf. Sci. 618 (2013) 3–11, https://doi.org/10.1016/j.susc.2013.09.009.
[45] C.D. Wagner, A. Joshi, The Auger parameter, its utility and advantages: a review, J. Electron Spectrosc. Relat. Phenom. 47 (1988) 283–313, https://doi.org/10.1016/0368-2048(88)85018-7.
[46] S.W. Gaarenstroom, N. Winograd, Initial and final state effects in the ESCA spectra of cadmium and silver oxides, J. Chem. Phys. (1977) 67, https://doi.org/10.1063/1.435347.
[47] F. Maldonado, A. Stashans, Al-doped ZnO : electronic, electrical and structural properties, J. Phys. Chem. Solids 71 (2010) 784–787, https://doi.org/10.1016/j.jpcs.2010.02.001.
[48] W. Körner, C. Elsässer, First-principles density functional study of dopant elements at grain boundaries in ZnO, Phys. Rev. B 81 (2010) 1–12, https://doi.org/10.1103/PhysRevB.81.085324.
[49] W. Ranke, Separation of the partial s- and p- densities of valence states of ZnO from UPS measurements, Solid State Commun. 19 (1976) 685–688, https://doi.org/10.1016/0038-1098(76)91105-4.
[50] W. Körner, C. Elsässer, Density functional theory study of dopants in polycrystalline TiO_2, Phys. Rev. B 205315 (2011) 1–11, https://doi.org/10.1103/PhysRevB.83.205315.
[51] P.B. Barna, M. Adamik, Fundamental structure forming phenomena of polycrystalline films and the structure zone models, Thin Solid Films 317 (1998) 27–33, https://doi.org/10.1016/S0040-6090(97)00503-8.
[52] A. Segmüller, M. Murakami, X-ray diffraction analysis of strains and stresses in thin films, Treatise Mater. Sci. Technol. (1988) 143–200, https://doi.org/10.1016/B978-0-12-341827-2.50010-8.
[53] H. Sowa, H. Ahsbahs, High-pressure X-ray investigation of zincite ZnO single crystals using diamond anvils with an improved shape, J. Appl. Crystallogr. 2489 (2006) 169–175, https://doi.org/10.1107/S0021889805042457.
[54] J. Idé, D. Cornil, A. Jacques, B. Navet, P. Boulanger, L. Ventelon, R. Lazzaroni, D. Beljonne, Glass hardness modification by means of ion implantation : electronic doping versus surface composition effect, Adv. Theory Simul. 1900039 (2019) 1–6, https://doi.org/10.1002/adts.201900039.
[55] I. Sieber, N. Wanderka, I. Urban, I. Dörfel, E. Schierhorn, F. Fenske, W. Fuhs, Electron microscopic characterization of reactively sputtered ZnO films with different Al-doping levels, Thin Solid Films 330 (1998) 108–113, https://doi.org/10.1016/S0040-6090(98)00608-7.
[56] A. Janotti, C.G. Van de Walle, Fundamentals of zinc oxide as a semiconductor, Rep. Prog. Phys. (2009), https://doi.org/10.1088/0034-4885/72/12/126501.
[57] A. Janotti, D. Segev, C.G. Van de Walle, Effects of cation d states on the structural and electronic properties of III-nitride and II-oxide wide-band-gap semiconductors, Phys. Rev. B 74 (2006) 1–9, https://doi.org/10.1103/PhysRevB.74.045202.
[58] R.M.V.S. Almeida, A.L. da Rosa, T. Frauenheim, J.S. de Almeida, Optoelectronic properties of zinc oxide: a first-principles investigation using the Tran-Blaha modified Becke-Johnson potential, Phys. Status Solidi Basic Res. 256 (2019), https://doi.org/10.1002/pssb.201800380.
[59] K. Osuch, E.B. Lombardi, W. Gebicki, First principles study of ferromagnetism in $Ti_{0.0625}Zn_{0.9375}O$, Phys. Rev. B Condens. Matter Mater. Phys. (2006) 73, https://doi.org/10.1103/PhysRevB.73.075202.
[60] J.P. Perdew, M. Levy, Physical content of the exact Kohn-Sham orbital energies: band gaps and derivative discontinuities, Phys. Rev. Lett. 51 (1983) 1884–1887, https://doi.org/10.1103/PhysRevLett.51.1884.
[61] S.H. Wei, A. Zunger, Role of metal *d* states in II–VI semiconductors, Phys. Rev. B (1988) 37, https://doi.org/10.1103/PhysRevB.37.8958.
[62] J. Tauc, R. Grigorovici, A. Vancu, Optical properties and electronic structure of amorphous germanium, Phys. Status Solidi 627 (1966) 627–637, https://doi.org/10.1002/pssb.19660150224.
[63] J. Tauc, A. Menth, States in the gap, J. Non Cryst. Solids 10 (1972) 569–585, https://doi.org/10.1016/0022-3093(72)90194-9.
[64] T.S. Moss, The interpretation of the properties of indium antimonide, Proc. Phys. Soc. B (1954) 775, https://doi.org/10.1088/0370-1301/67/10/306.
[65] E. Burstein, Anomalous optical absorption limit in InSb, Phys. Rev. 93 (1954) 632–633, https://doi.org/10.1103/PhysRev.93.632.